GEOPHYSICS, VOL. 80, NO. 2 (MARCH-APRIL 2015); P. IM35–IM44, 9 FIGS.
10.1190/GEO2014-0323.1

3D seismic image processing for unconformities

Xinming Wu[1] and Dave Hale[1]

ABSTRACT

In seismic images, an unconformity can be first identified by reflector terminations (i.e., *truncation, toplap, onlap, or downlap*), and then it can be traced downdip to its corresponding correlative conformity, or updip to a parallel unconformity; for example, in topsets. Unconformity detection is a significant aspect of seismic stratigraphic interpretation, but most automatic methods work only in 2D and can only detect angular unconformities with reflector terminations. Moreover, unconformities pose challenges for automatic techniques used in seismic interpretation. First, it is difficult to accurately estimate normal vectors or slopes of seismic reflectors at an unconformity with multioriented structures due to reflector terminations. Second, seismic flattening methods cannot correctly flatten reflectors at unconformities that represent hiatuses or geologic age gaps. We have developed a 3D unconformity attribute computed from a seismic amplitude image to detect unconformities by highlighting the angular unconformities and corresponding parallel unconformities or correlative conformities. These detected unconformity surfaces were further used as constraints for a structure-tensor method to more accurately estimate seismic normal vectors at unconformities. Finally, using detected unconformities as constraints and more accurate normal vectors, we could better flatten seismic images with unconformities.

INTRODUCTION

An unconformity is a nondepositional or erosional surface separating older strata below from younger strata above, and thus it represents a significant gap in the rock record (Vail et al., 1977). Unconformity extraction from seismic images is important for seismic stratigraphic interpretation because unconformities represent discontinuities in otherwise continuous deposits and hence serve as boundaries when interpreting seismic sequences that represent successively deposited layers.

In addition, the detected unconformities can be applied as constraints to improve a structure-tensor method (Van Vliet and Verbeek, 1995; Fehmers and Höcker, 2003) for more accurately estimating normal vectors of seismic reflectors at unconformities with multioriented structures, and improve a seismic image flattening method (Lomask et al., 2006; Parks, 2010; Luo and Hale, 2013; Wu and Hale, 2014) to more accurately flatten reflectors at unconformities with geologic age gaps.

Unconformity detection

Seismic coherence (Bahorich and Farmer, 1995), which highlights reflector discontinuities, is commonly used to detect faults, channel edges, and other lateral changes in waveform. Although sensitive to unconformities, coherence vertically smears the response over the computation window and unconformities usually appear as vertical changes in the waveform. Barnes et al. (2000) and Hoek et al. (2010) propose an unconformity attribute that measures the degree of seismic reflector convergence (or divergence), and thereby highlights the termination areas of an unconformity. Smythe et al. (2004) introduce a spectral image of correlative events attribute to obtain stratigraphic details by highlighting discontinuities in band-limited seismic data. All of these methods process a seismic image locally (Ringdal, 2012) to compute unconformity attributes that can highlight an unconformity within its termination area but cannot detect its corresponding parallel unconformities or correlative conformities.

Ringdal (2012) proposes a global method that first extracts a 2D flow field that is everywhere tangent to reflectors in a 2D seismic image. Then, the flow field is used to compute an unconformity probability image by repeating the following processing for each sample: (1) Four seeds are first placed at the four neighbors of the sample in the 2D flow field, (2) the four seeds then move along the flow field to produce trajectories, (3) the separation rate of the trajectories is calculated, and (4) this separation is converted to an

Manuscript received by the Editor 14 July 2014; revised manuscript received 6 October 2014; published online 2 February 2015; corrected version published online 12 February 2015.
[1]Colorado School of Mines, Golden, Colorado, USA. E-mail: xinwu@mines.edu; dhale@mines.edu.

unconformity probability for that sample. The advantage of this method is that it can detect a parallel unconformity or correlative conformity using long trajectories that extend from the parallel unconformity or correlative conformity to the corresponding angular unconformity. The disadvantage is that, to detect such a correlative conformity or parallel unconformity, the trajectories are required to start from the parallel area (parallel unconformity highlighted by the blue ellipse in Figure 1a) and end in the nonparallel area (termination highlighted by the green ellipse in Figure 1a). Another disadvantage is that the trajectory extraction along a flow field applies only for 2D images. For 3D seismic images, this method processes inline and crossline slices separately throughout the volume to compute an unconformity probability volume.

Seismic normal vector estimation at unconformities

Orientation vector fields, such as vectors normal to or slopes of seismic reflectors, are useful for seismic interpretation. For example, estimated orientation information is used to control slope-based (Fomel, 2002) and structure-oriented (Fehmers and Höcker, 2003; Hale, 2009) filters, so that they smooth along reflectors to enhance their coherencies. Seismic normal vectors or slopes are also used to track horizons (de Groot et al., 2010) and to flatten (Lomask et al., 2006; Parks, 2010) or unfold (Luo and Hale, 2013) seismic images, or to generate horizon volumes (Wu and Hale, 2014).

Structure tensors (Van Vliet and Verbeek, 1995; Fehmers and Höcker, 2003) or plane-wave destruction filters (Fomel, 2002) have been proposed to estimate seismic normal vectors or slopes. These methods can accurately estimate orientation vectors for structures with only one locally dominant orientation. This means that they can correctly estimate the normal vectors (or slopes) of the reflectors in conformable areas of a seismic image, but for an angular unconformity where two different structures meet, these methods yield smoothed vectors that represent averages of orientations across the unconformity.

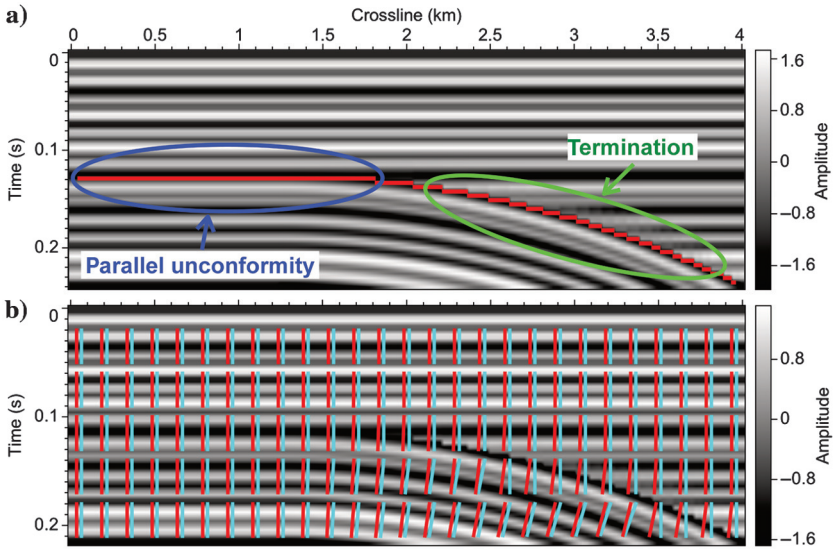

Figure 1. A 2D synthetic seismic image (a) with an unconformity (red curve) that is manually interpreted from the termination area to its corresponding parallel unconformity. The estimated seismic normal vectors (red segments in [b]) are smoothed within the termination area, and therefore they are incorrect, compared with the true seismic normal vectors (cyan segments in [b]) that are discontinuous within that area.

Seismic image flattening at unconformities

Seismic image flattening (Lomask et al., 2006; Parks, 2010; Wu and Hale, 2014) or unfolding (Luo and Hale, 2013) methods are applied to a seismic image to obtain a flattened image, in which all seismic reflectors are horizontal. From such a flattened seismic image, all seismic horizons can be identified by slicing horizontally.

Extracting horizons terminated by faults or unconformities is generally difficult for these methods. Luo and Hale (2013) extract horizons across faults by first unfaulting a seismic image; Wu and Hale (2014) do the same by placing control points on opposite sides of faults. However, none of these methods correctly flattens a seismic image with unconformities, which should produce gaps in the flattened image. Wu and Zhong (2012a, 2012b) flatten a seismic image with unconformities using a relative geologic time (RGT) volume generated with a phase unwrapping method, but all the unconformities in the seismic image have to be manually interpreted to constrain the phase unwrapping.

This paper

In this paper, we first propose a method to automatically detect an unconformity, complete with its termination area and corresponding parallel unconformities or correlative conformities. We then estimate seismic normal vectors at unconformities using the detected unconformities as constraints. Finally, we flatten seismic images containing unconformities using these estimated seismic normal vectors and constraints derived from detected unconformities.

UNCONFORMITY DETECTION

In manual 3D seismic stratigraphic interpretation, an unconformity is first recognized as a boundary where seismic reflectors terminate by truncation, toplap, onlap, or downlap, and then is traced into parallel reflections either downdip to its correlative conformity or updip into topsets. Therefore, to obtain a complete unconformity, an automatic method should be able to detect the termination areas (green ellipse in Figure 1a) and parallel unconformities (blue ellipse in Figure 1a) or correlative conformities corresponding to the unconformity.

We propose an unconformity attribute that measures differences between two seismic normal vector fields computed from two structure-tensor fields. The first structure-tensor field is computed using a vertically causal smoothing filter. The second one is computed using a vertically anticausal smoothing filter. This attribute can detect an unconformity by highlighting its termination areas and its corresponding parallel unconformities or correlative conformities.

Structure tensor

The structure tensor (Van Vliet and Verbeek, 1995; Fehmers and Höcker, 2003) can be used to estimate seismic normal vectors that are perpendicular to seismic reflectors. For a 2D image, the structure tensor $\mathbf{T}$ for each sample is a 2×2 symmetric positive-semidefinite matrix constructed as the smoothed outer product of image gradients:

$$\mathbf{T} = \langle \mathbf{g}\mathbf{g}^{\top} \rangle_{h,v} = \begin{bmatrix} \langle g_1 g_1 \rangle_{h,v} & \langle g_1 g_2 \rangle_{h,v} \\ \langle g_1 g_2 \rangle_{h,v} & \langle g_2 g_2 \rangle_{h,v} \end{bmatrix}, \quad (1)$$

where $\mathbf{g} = [g_1 \ g_2]^{\top}$ represents the image gradient vector computed for each image sample, $\langle \cdot \rangle_{h,v}$ represents smoothing for each outer-product element in the horizontal (subscript h) and vertical (subscript v) directions. These horizontal and vertical smoothing filters are implemented with 1D recursive Gaussian filters (Hale, 2006) with corresponding half-widths σ_h and σ_v.

As shown by Fehmers and Höcker (2003), the seismic normal vector for each image sample can be estimated from the eigendecomposition of the structure tensor $\mathbf{T}$:

$$\mathbf{T} = \lambda_u \mathbf{u}\mathbf{u}^{\top} + \lambda_v \mathbf{v}\mathbf{v}^{\top}, \quad (2)$$

where $\mathbf{u}$ and $\mathbf{v}$ are unit eigenvectors corresponding to eigenvalues λ_u and λ_v of $\mathbf{T}$.

We choose $\lambda_u \geq \lambda_v$, so that the eigenvector $\mathbf{u}$, which corresponds to the largest eigenvalue λ_u, indicates the direction of highest change in image amplitude, and therefore it is perpendicular to locally linear features in an image, whereas the orthogonal eigenvector $\mathbf{v}$ indicates the direction that is parallel to such features. In other words, eigenvector $\mathbf{u}$ is the seismic normal vector that is perpendicular to seismic reflectors in a seismic image, and eigenvector $\mathbf{v}$ is parallel to the reflectors.

Smoothing

The structure tensor $\mathbf{T}$ given in equation 1 can be used to accurately estimate the local orientation of structures in an image in which there is only one locally dominant orientation present. However, for multioriented structures, such as an unconformity at which seismic reflectors terminate (green ellipse in Figure 1a), this structure tensor provides a local average of the orientations of structures. The seismic normal vectors (red segments in Figure 1b) estimated from $\mathbf{T}$ are smoothed near the termination area, whereas the true normal vectors (cyan segments in Figure 1b) are discontinuous across the unconformity.

At an unconformity where seismic reflectors terminate (green ellipse in Figure 1a), structures of reflectors above the unconformity are different from those of reflectors below. Therefore, if we compute structure tensors using vertically causal smoothing filters, which average structures from above, we will obtain normal vectors at the unconformity that are different from those obtained using vertical anticausal filters, which average structures from below.

With a vertically causal filter, the structure tensor computed for each sample represents structures averaged using only samples above. We define such a structure tensor as

$$\mathbf{T}_c = \begin{bmatrix} \langle g_1 g_1 \rangle_{h,vc} & \langle g_1 g_2 \rangle_{h,vc} \\ \langle g_1 g_2 \rangle_{h,vc} & \langle g_2 g_2 \rangle_{h,vc} \end{bmatrix}, \quad (3)$$

where $\langle \cdot \rangle_{h,vc}$ represents horizontal Gaussian (subscript h) and vertically causal (subscript vc) smoothing filters.

With a vertically anticausal filter, the structure tensor computed for each sample represents structures averaged using only samples below. We define such a structure tensor as

$$\mathbf{T}_a = \begin{bmatrix} \langle g_1 g_1 \rangle_{h,va} & \langle g_1 g_2 \rangle_{h,va} \\ \langle g_1 g_2 \rangle_{h,va} & \langle g_2 g_2 \rangle_{h,va} \end{bmatrix}, \quad (4)$$

where the subscript va denotes a vertically anticausal smoothing filter.

Vertical smoothing

To compute two structure-tensor fields that differ significantly at an unconformity, the causal smoothing filter that averages from above should smooth along the direction perpendicular to the structures above the unconformity, whereas the anticausal filter should smooth along the direction perpendicular to the structures below the unconformity. Here, we use vertically causal and anticausal filters because unconformities tend to be close to horizontal in seismic images. We implement these two filters with one-sided exponential smoothing filters, which are efficient and trivial to implement.

A one-sided causal exponential filter for input and output sequences `x[i]` and `y[i]` with lengths n can be implemented in C++ (or Java) as follows:

```
float b = 1.0f-a;
float yi = y[0] = x[0];
for (int i=1; i<n; ++i)
  y[i] = yi = a*yi+b*x[i].
```

Similarly, a one-sided anticausal exponential filter can be implemented as follows:

```
float b = 1.0f-a;
float yi = y[n-1] = x[n-1];
for (int i=n-2; i>=0; --i)
  y[i] = yi = a*yi+b*x[i].
```

The parameter `a` in these two one-sided exponential filters controls the extent of smoothing. In all examples, we use `a = 0.8`, which for low frequencies approximates a half-Gaussian filter with half-width $\sigma = 6$ samples.

From structure-tensor fields, $\mathbf{T}_c$ and $\mathbf{T}_a$ computed for the same seismic image using vertically causal and anticausal smoothing filters, respectively, we estimate two seismic normal vector fields $\mathbf{u}_c$ and $\mathbf{u}_a$. As shown in Figure 2a, the two seismic normal vector fields $\mathbf{u}_c$ (green segments in Figure 2a) and $\mathbf{u}_a$ (yellow segments in Figure 2a) are identical in conformable areas with parallel seismic reflectors because the orientation of structures locally averaged from above (used to compute $\mathbf{T}_c$) is identical to the orientation of structures averaged from below (used to compute $\mathbf{T}_a$). However, at the termination area of an unconformity, the two vector fields are different because the structure tensors $\mathbf{T}_c$ computed with structures locally averaged from above should be different from $\mathbf{T}_a$ computed with structures locally averaged from below.

Therefore, as shown in Figure 2a, the difference between estimated normal vector fields $\mathbf{u}_c$ and $\mathbf{u}_a$ provides a good indication of the termination area of an unconformity. However, a complete unconformity, that is, a curve (in 2D) or surface (in 3D) with geologic age gaps, extends from its termination area updip or downdip into parallel reflectors. Thus, we should extend normal vector differences from the termination area, where these differences originate, into the corresponding parallel unconformity or correlative conformity.

Structure-oriented smoothing

To detect a correlative conformity or parallel unconformity, we extend vector differences (between $\mathbf{u}_c$ and $\mathbf{u}_a$) at an unconformity from its termination area to its correlative conformity or parallel unconformity, by replacing the horizontal Gaussian smoothing filter in equations 3 and 4 with a structure-oriented smoothing filter (Hale, 2009) when computing structure tensors.

Then, the structure tensors $\mathbf{T}_{s,c}$ and $\mathbf{T}_{s,a}$, computed with a laterally structure-oriented filter and vertically causal and anticausal filters, are defined by

$$\mathbf{T}_{s,c} = \begin{bmatrix} \langle g_1 g_1 \rangle_{s,vc} & \langle g_1 g_2 \rangle_{s,vc} \\ \langle g_1 g_2 \rangle_{s,vc} & \langle g_2 g_2 \rangle_{s,vc} \end{bmatrix}, \tag{5}$$

and

$$\mathbf{T}_{s,a} = \begin{bmatrix} \langle g_1 g_1 \rangle_{s,va} & \langle g_1 g_2 \rangle_{s,va} \\ \langle g_1 g_2 \rangle_{s,va} & \langle g_2 g_2 \rangle_{s,va} \end{bmatrix}, \tag{6}$$

where the subscript s represents a structure-oriented filter that smooths along reflectors in a seismic image. Note that the structure-oriented smoothing is generally more expensive than the vertically causal and anticausal smoothing. We therefore first apply the structure-oriented smoothing filter to each element of $\mathbf{g}\mathbf{g}^{\mathsf{T}}$ to obtain $\mathbf{T}_s = \langle \mathbf{g}\mathbf{g}^{\mathsf{T}} \rangle_s$, which then is smoothed separately by vertically causal and anticausal filters to obtain $\mathbf{T}_{s,c}$ and $\mathbf{T}_{s,a}$, respectively. By doing this, we apply the relatively expensive structure-oriented smoothing only once. However, if we first apply the vertically causal and anticausal smoothing to compute the two differently smoothed outer products $\langle \mathbf{g}\mathbf{g}^{\mathsf{T}} \rangle_c$ and $\langle \mathbf{g}\mathbf{g}^{\mathsf{T}} \rangle_a$, we then need to apply the structure-oriented smoothing twice to obtain two structure-tensor fields $\mathbf{T}_{s,c}$ and $\mathbf{T}_{s,a}$.

As discussed by Hale (2009, 2011), to obtain a smoothed output image $q(\mathbf{x})$ from an input $p(\mathbf{x})$, the structure-oriented smoothing method solves a finite-difference approximation to the following partial differential equation:

$$q(\mathbf{x}) - \frac{\sigma^2}{2} \nabla \cdot \mathbf{D}(\mathbf{x}) \cdot \nabla q(\mathbf{x}) = p(\mathbf{x}), \tag{7}$$

where $\mathbf{D}(\mathbf{x})$ is a diffusion-tensor field that shares the eigenvectors of the structure tensor computed from an image, and therefore orients the smoothing along image structures. Similar to the half-width σ in a Gaussian smoothing filter, the parameter σ controls the extent of smoothing.

In 2D, we use the eigenvectors $\mathbf{u}(\mathbf{x})$ and $\mathbf{v}(\mathbf{x})$, estimated using the structure tensors shown in equation 1, to construct our diffusion-tensor field:

$$\mathbf{D}(\mathbf{x}) = \lambda_u(\mathbf{x})\mathbf{u}(\mathbf{x})\mathbf{u}^{\mathsf{T}} + \lambda_v(\mathbf{x})\mathbf{v}(\mathbf{x})\mathbf{v}^{\mathsf{T}}(\mathbf{x}). \tag{8}$$

Then, because eigenvectors $\mathbf{u}(\mathbf{x})$ and $\mathbf{v}(\mathbf{x})$ are perpendicular and parallel to seismic reflectors, respectively, we can control the structure-oriented filter to smooth along reflectors by setting the corresponding eigenvalues $\lambda_u(\mathbf{x}) = 0$ and $\lambda_v(\mathbf{x}) = 1$ for all tensors in $\mathbf{D}(\mathbf{x})$. In 3D, a structure tensor $\mathbf{T}$ for each image sample is a 3×3 matrix, from which the eigendecomposition provides three eigenvectors $\mathbf{u}$, $\mathbf{v}$, and $\mathbf{w}$, where $\mathbf{u}$ is orthogonal to locally planar features and $\mathbf{v}$ and $\mathbf{w}$ lie within the planes of any locally planar features. We then construct the structure-oriented diffusion-tensor field in 3D as $\mathbf{D}(\mathbf{x}) = \lambda_u(\mathbf{x})\mathbf{u}(\mathbf{x})\mathbf{u}^{\mathsf{T}}(\mathbf{x}) + \lambda_v(\mathbf{x})\mathbf{v}(\mathbf{x})\mathbf{v}^{\mathsf{T}}(\mathbf{x}) + \lambda_w(\mathbf{x})\mathbf{w}(\mathbf{x})\mathbf{w}^{\mathsf{T}}(\mathbf{x})$, and set $\lambda_u(\mathbf{x}) = 0$ and $\lambda_v(\mathbf{x}) = \lambda_w(\mathbf{x}) = 1$, so that the filter diffuses or smooths image features along structures.

As indicated by the seismic normal vectors shown in Figure 1b, normal vectors (red segments) estimated using the structure tensors computed in equation 1 are inaccurate at unconformities. However, they are accurate in conformable areas, including the area near the parallel unconformity. Thus, the structure tensors in equation 1 are adequate for constructing diffusion tensors $\mathbf{D}(\mathbf{x})$ for structure-oriented smoothing along seismic reflectors, including those near the parallel unconformity and correlative conformity corresponding to an unconformity. As discussed in Hale (2009), using structure-oriented diffusion tensors $\mathbf{D}(\mathbf{x})$ for the smoothing filter in equation 7, the smoothing-filter weights are largest along curvilinear trajectories that coincide with image structures, which means that the filter diffuses or extends image values from high to low along structures. Therefore, by applying such a structure-oriented filter to the elements of the structure tensors $\mathbf{T}_{s,c}$ and $\mathbf{T}_{s,a}$, the structure-oriented smoothing filter weights extend structural differences, originating within the termination area of an unconformity, into the corresponding parallel unconformity and correlative conformity. Because σ in equation 7 controls the extent of smoothing, to detect parallel unconformities or correlative conformities that extend long away from an angular unconformity, we need to use a large σ. In practice, we use $\sigma = n_x$ for 2D and $\sigma = \max(n_x, n_y)$ for 3D, where n_x and n_y are

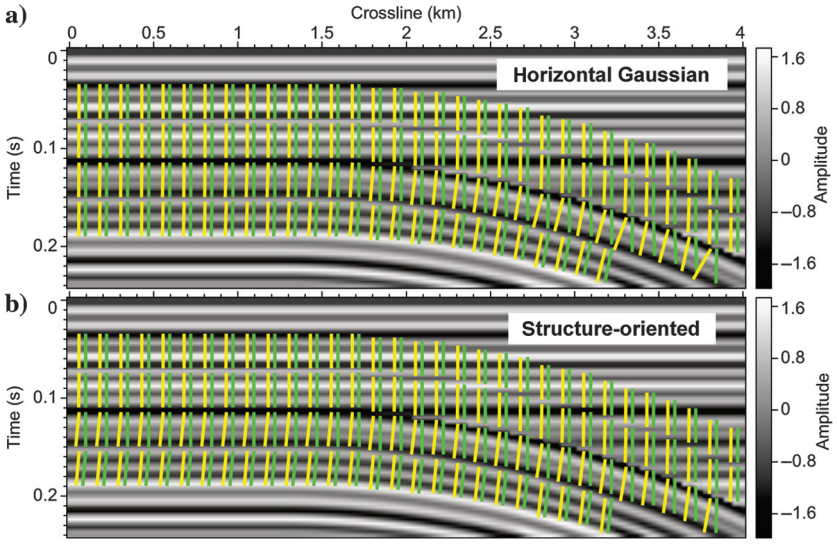

Figure 2. Two different seismic normal vector fields estimated using structure tensors computed with vertically causal (green segments) and anticausal (yellow segments) smoothing filters. In panel (a), the vector fields differ only within the termination area of the unconformity, and in panel (b), these vector differences are extended to the parallel unconformity.

the number of samples in the horizontal dimensions of an input seismic image.

As shown in Figure 2, using structure tensors $\mathbf{T}_c$ and $\mathbf{T}_a$ computed with a horizontal Gaussian filter and vertically causal and anticausal filters, the estimated seismic normal vectors $\mathbf{u}_c$ (green segments in Figure 2a) and $\mathbf{u}_a$ (yellow segments in Figure 2a) differ only within the termination area of the unconformity. Using structure tensors $\mathbf{T}_{s,c}$ and $\mathbf{T}_{s,a}$ computed with a structure-oriented smoothing filter instead of a horizontal Gaussian filter, the differences between the estimated seismic normal vectors $\mathbf{u}_{s,c}$ (green segments in Figure 2b) and $\mathbf{u}_{s,a}$ (yellow segments in Figure 2b) are extended from the termination area to the parallel unconformity.

In summary, by first applying a structure-oriented filter to each structure-tensor element of $\mathbf{g}\mathbf{g}^{\mathsf{T}}$, we extend any structure differences, which originate within the termination area of an unconformity, to its corresponding parallel unconformity and correlative conformity. Then, applying vertically causal and anticausal filters for each structure-tensor element, we compute two different structure-tensor fields $\mathbf{T}_{s,c}$ and $\mathbf{T}_{s,a}$ with seismic normal vector fields $\mathbf{u}_{s,c}$ and $\mathbf{u}_{s,a}$ that differ within the termination area and the corresponding correlative conformity and parallel unconformity. Finally, the differences between the two estimated vector fields $\mathbf{u}_{s,c}$ and $\mathbf{u}_{s,a}$ can be used as an unconformity attribute that highlights the angular unconformity and its corresponding parallel unconformities or correlative conformities.

Unconformity likelihood

As shown in Figure 2b, the vectors $\mathbf{u}_{s,c}$ (green segments) and $\mathbf{u}_{s,a}$ (yellow segments) are identical everywhere except at the unconformity, including its termination area and parallel unconformity. Therefore, we define an *unconformity likelihood* attribute g, that evaluates the differences between $\mathbf{u}_{s,c}$ and $\mathbf{u}_{s,a}$, to highlight unconformities:

$$g \equiv 1 - (\mathbf{u}_{s,c} \cdot \mathbf{u}_{s,a})^p. \tag{9}$$

The power $p(p > 1)$ is used to increase the contrast between samples with low and high unconformity likelihoods.

Using a process similar to that used by Hale (2012) for extracting ridges of fault likelihoods, we extract ridges of unconformity likelihood by scanning each vertical column of the unconformity likelihood image (Figures 3a and 4a), preserving only local maxima, and setting unconformity likelihoods elsewhere to zero. Figures 3b and 4b show that ridges of unconformity likelihood coincide with the unconformity that appears in the synthetic seismic image.

For a 3D seismic image, following the same process as above, we compute an unconformity likelihood volume as shown in Figure 5, which correctly highlights two apparent unconformities. In the time slices of unconformity likelihoods before (Figure 5a) and after (Figure 5b) thinning, we observe that samples in the lower-left and upper-right areas, separated by high unconformity likelihoods, suggest different seismic facies. This indicates that they belong to two different depositional sequences that have different geologic ages.

From ridges of unconformity likelihoods (Figure 5b), we connect adjacent samples with high unconformity likelihoods to form unconformity surfaces as shown in the upper-right panel of Figure 5b.

APPLICATIONS

We first use unconformity likelihoods as constraints to more accurately estimate seismic normal vectors at unconformities. Then, using more accurate normal vectors and unconformity likelihoods as constraints in our seismic image flattening method, we are able to better flatten an image containing unconformities.

Estimation of seismic normal vectors at unconformities

Using structure tensors computed with horizontal and vertical Gaussian filters as shown in equation 1, we find smoothed seismic normal vectors (red segments in Figure 1b) in the termination area because discontinuous structures across the unconformity are smoothed by symmetric Gaussian filters. Therefore, to obtain correct normal vectors (cyan segments in Figure 1b) that are discontinuous in the termination area, we must use more appropriate filters to compute structure tensors.

To preserve structure discontinuities, we compute the structure tensors using horizontal and vertical filters that do not smooth across unconformities:

$$\mathbf{T} = \begin{bmatrix} \langle g_1 g_1 \rangle_{sh,sv} & \langle g_1 g_2 \rangle_{sh,sv} \\ \langle g_1 g_2 \rangle_{sh,sv} & \langle g_2 g_2 \rangle_{sh,sv} \end{bmatrix}, \tag{10}$$

where $\langle \cdot \rangle_{sh,sv}$ represent the horizontal (subscript sh) and vertical (subscript sv) filters that vary spatially, and for which the extent of smoothing is controlled by the thinned unconformity likelihoods.

The horizontal and vertical filters are similar to the edge-preserving smoothing filter discussed in Hale (2011):

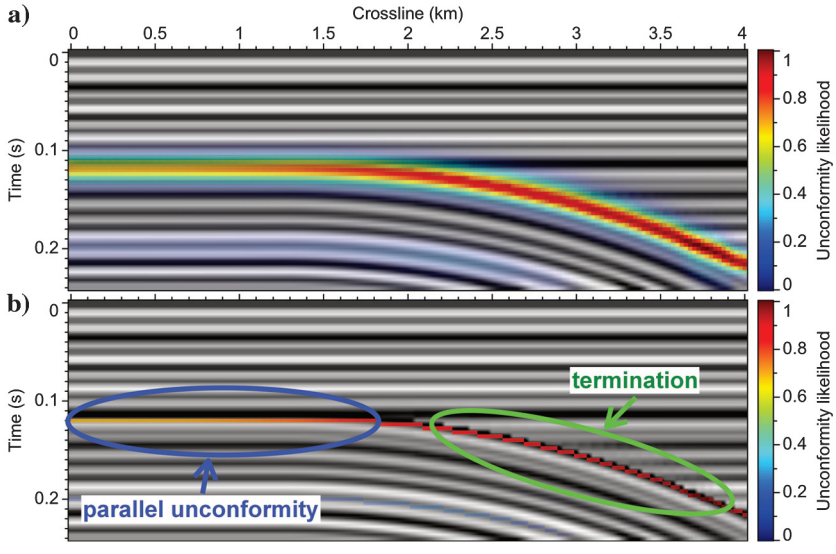

Figure 3. Unconformity likelihoods, an attribute that evaluates differences between two estimated seismic normal vector fields (yellow and green segments in Figure 2b), before (a) and after (b) thinning highlight the termination area and parallel unconformity.

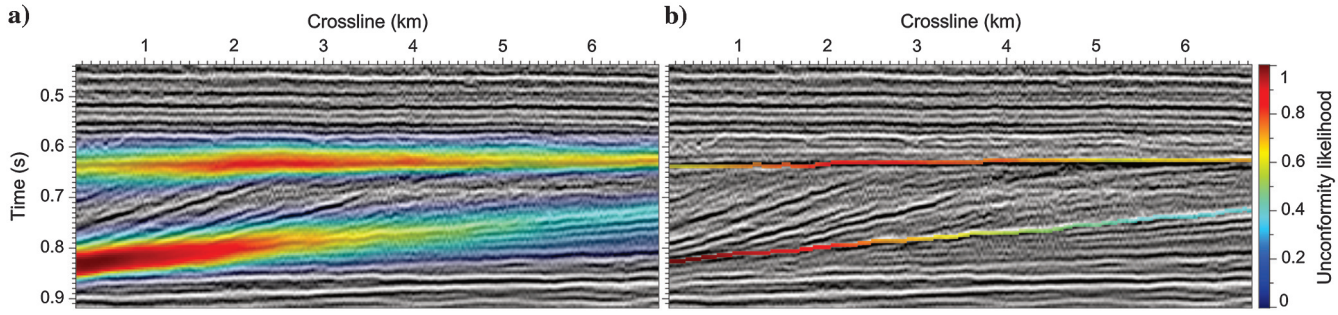

Figure 4. Unconformity likelihoods (a) before and (b) after thinning.

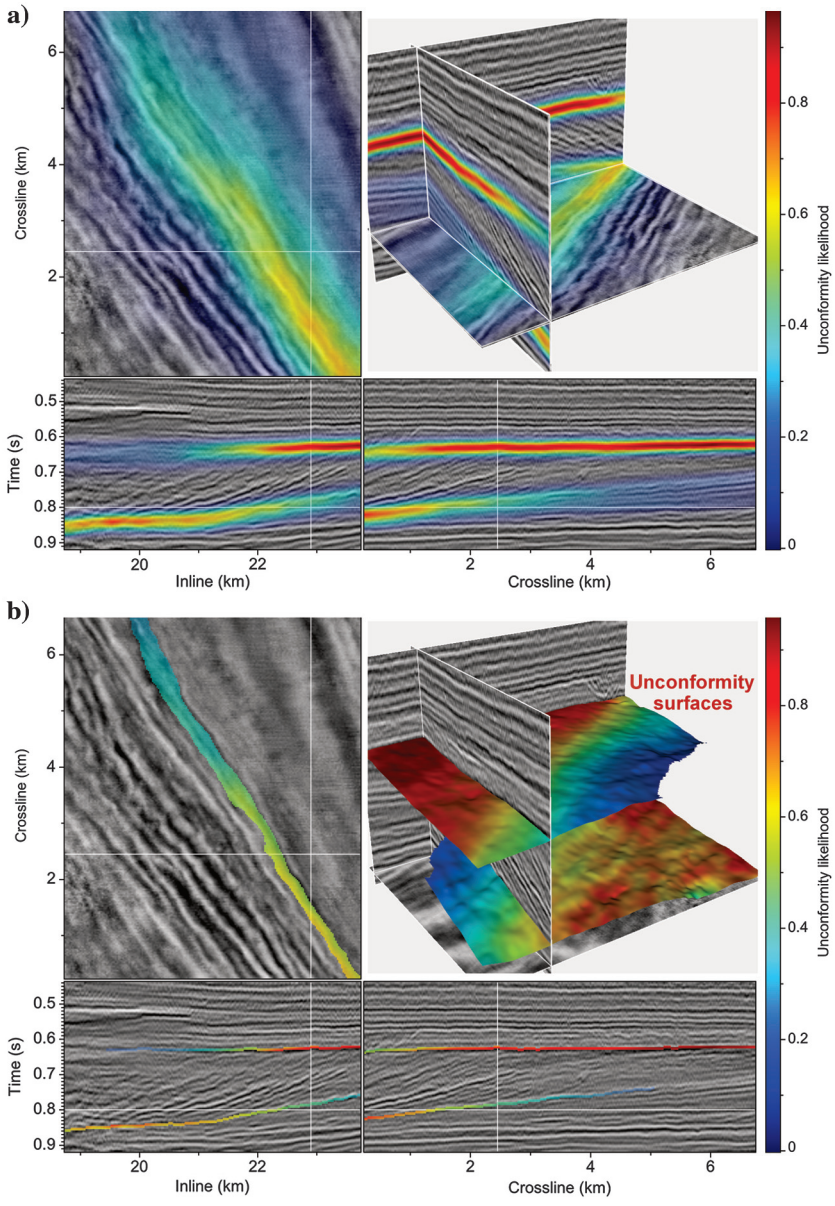

Figure 5. Unconformity likelihoods (a) before and (b) after thinning. Thinned unconformity likelihoods form unconformity surfaces as shown in the top-right panel in panel (b).

$$q(\mathbf{x}) - \frac{\sigma^2}{2}\nabla \cdot c^2(\mathbf{x}) \cdot \nabla q(\mathbf{x}) = p(\mathbf{x}). \quad (11)$$

We compute $c(\mathbf{x}) = 1 - g_t(\mathbf{x})$ to prevent this filter from smoothing across unconformities. Here, $g_t(\mathbf{x})$ is a thinned unconformity likelihood image as shown in Figure 4b that has large values (close to one) only at unconformities and zeros elsewhere.

Figure 6a and 6d shows vertical and horizontal components of the true normal vectors for the synthetic image shown in Figure 1a. We observe that the two components are discontinuous at the unconformity. However, using the conventional structure-tensor method as in equation 1, the two components (Figure 6b and 6e) of the estimated seismic normal vectors are smooth, and therefore they are inaccurate at the unconformity. Using the improved structure-tensor method constrained by the unconformity likelihoods (Figure 3) as in equation 10, the estimated seismic normal vectors shown in Figure 6c and 6f are almost the same as the true ones shown in Figure 6a and 6d.

Figure 7 shows seismic normal vectors estimated for the image with two unconformities shown in Figure 4. The vertical (Figure 7a) and horizontal (Figure 7c) components of seismic normal vectors, estimated from structure tensors computed as in equation 1, are smooth at the unconformities; those estimated from structure tensors computed as in equation 10 preserve discontinuities at unconformities (Figure 7b and 7d).

Seismic image flattening at unconformities

Seismic normal vectors or slopes can be used to flatten (Lomask et al., 2006; Parks, 2010) or unfold (Luo and Hale, 2013) a seismic image to generate a horizon volume (Wu and Hale, 2014), that allows for the extraction of all seismic horizons in the image. However, neither of these methods correctly flatten seismic images with unconformities for two reasons: First, estimated

seismic normal vectors or slopes of seismic reflectors are inaccurate at unconformities with multioriented structures. Second, seismic reflectors or horizons terminate at unconformities that represent geologic age gaps.

In this paper, we have proposed methods to automatically detect unconformities and more accurately estimate seismic normal vectors at unconformities. Therefore, we can easily extend the flattening method described in Wu and Hale (2014), to better flatten a seismic image at unconformities, using seismic normal vectors estimated from structure tensors computed with equation 10, and by incorporating constraints derived from unconformity likelihoods into the flattening method. We incorporate unconformity constraints in our flattening method by weighting the equations for flattening using unconformity likelihoods, and then using the unconformity likelihoods to construct a preconditioner in the conjugate gradient method used to solve those equations.

Weighting

To generate a horizon volume or to flatten a seismic image, we first solve for vertical shifts $s(x, y, z)$ as discussed in Wu and Hale (2014):

$$\begin{bmatrix} w\left(-\frac{\partial s}{\partial x} - p\frac{\partial s}{\partial z}\right) \\ w\left(-\frac{\partial s}{\partial y} - q\frac{\partial s}{\partial z}\right) \\ \epsilon\frac{\partial s}{\partial z} \end{bmatrix} \approx \begin{bmatrix} wp \\ wq \\ 0 \end{bmatrix}, \tag{12}$$

where $p(x, y, z)$ and $q(x, y, z)$ are inline and crossline reflector slopes computed from seismic normal vectors; $w(x, y, z)$ represent weights for the equations; and the third equation $\epsilon(\partial s/\partial z) \approx 0$,

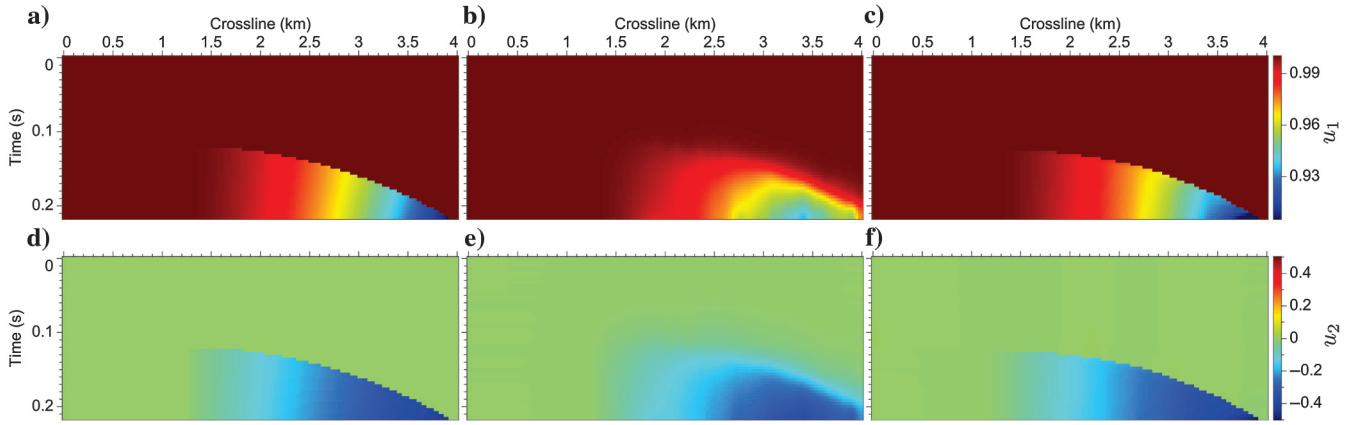

Figure 6. (a and d) Vertical (u_1) and horizontal (u_2) components of the true normal vectors of the synthetic image (Figure 1a), (c and f) the estimated normal vectors with the detected unconformity (Figure 3b) as constraints are more accurate than those, and (b and e) without constraints.

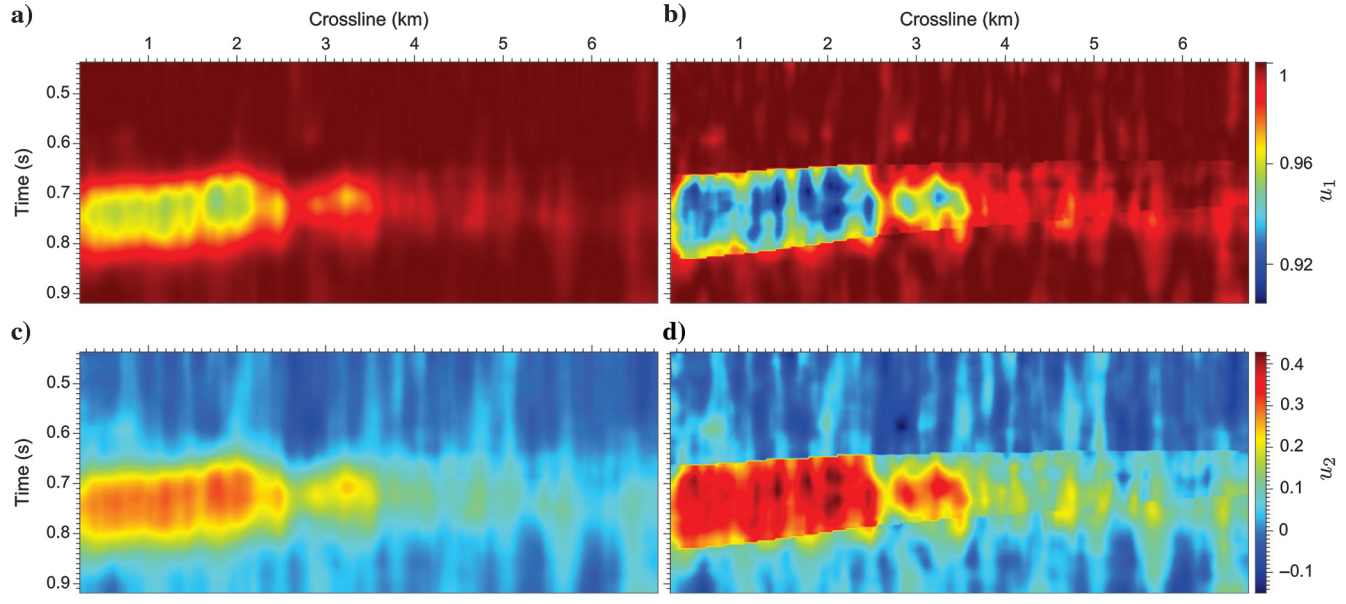

Figure 7. From the seismic image as shown in Figure 4, the vertical (u_1) and horizontal (u_2) components of seismic normal vectors (b and d) estimated using structure tensors computed with and (a and c) without unconformity constraints.

scaled by a small constant ϵ, is used to reduce rapid vertical variations in the shifts.

For a seismic image with unconformities, we incorporate constraints derived from unconformity likelihoods into equations 12 by setting $w(x,y,z) = 1 - g_t(x,y,z)$, and we use a spatially variant $\epsilon(x,y,z)$ instead of a constant value:

$$\epsilon(x,y,z) = \epsilon_0[1 - g_t(x,y,z)], \tag{13}$$

where ϵ_0 is a small constant number (we use $\epsilon_0 = 0.01$ for all examples in this paper) and $g_t(x,y,z)$ denotes the thinned unconformity likelihoods, such as those shown in Figure 5b.

This spatially variant $\epsilon(x,y,z)$, with smaller values (nearly zero) at unconformities, helps to generate more reasonable shifts with gradual variations everywhere except at unconformities.

Preconditioner

As discussed in Wu and Hale (2014), to obtain the shifts $s(x,y,z)$ in equation 12 for a 3D seismic image with N samples, we solve its corresponding least-squares problem expressed in a matrix form:

$$(\mathbf{WG})^\top \mathbf{WGs} = (\mathbf{WG})^\top \mathbf{Wv}, \tag{14}$$

where $\mathbf{s}$ is an $N \times 1$ vector containing the unknown shifts $s(x,y,z)$, $\mathbf{G}$ is a $3N \times N$ sparse matrix representing finite-difference approximations of partial derivatives, $\mathbf{W}$ is a $3N \times 3N$ diagonal matrix containing weights $w(x,y,z)$ and $\epsilon(x,y,z)$, $\mathbf{v}$ is a $3N \times 1$ vector with $2N$ slopes p and q, and N zeros.

Because the matrix $(\mathbf{WG})^\top \mathbf{WG}$ is symmetric positive-semidefinite, we can solve the linear system of equation 14 using the preconditioned conjugate gradient method, with a preconditioner $\mathbf{M}^{-1}$ as in Wu and Hale (2014):

$$\mathbf{M}^{-1} = \mathbf{S}_x\mathbf{S}_y\mathbf{S}_z\mathbf{S}_z^\top\mathbf{S}_y^\top\mathbf{S}_x^\top, \tag{15}$$

where $\mathbf{S}_x, \mathbf{S}_y$ and $\mathbf{S}_z$ are filters that smooth in the x-, y-, and z-directions, respectively.

For a seismic image with unconformities, the filters $\mathbf{S}_x, \mathbf{S}_y$ and $\mathbf{S}_z$ are spatially variant filters designed as in equation 11, to preserve discontinuities in shifts $s(x,y,z)$ at unconformities.

Results

With the computed shifts $s(x,y,z)$, we first generate an RGT volume $\tau(x,y,z) = z + s(x,y,z)$ (Figures 8a and 9a). We then use the RGT volume to map a seismic image $f(x,y,z)$ (Figure 4 or 5) in the depth-space domain to a flattened image $\tilde{f}(x,y,\tau)$ (Figure 8b or 9b) in the RGT-space domain.

From the 2D example shown in Figure 8, the RGT (Figure 8a) and flattened (Figure 8c) images, generated with inaccurate seismic normal vectors (Figure 7a and 7c) and without unconformity constraints, are incorrect at unconformities, where we expect discontinuities in the RGT image and corresponding gaps in the flattened image. With more accurate seismic normal vectors (Figure 7b and 7d) and with constraints derived from unconformity likelihoods (Figure 4), we obtain an improved RGT image (Figure 8b) with discontinuities at unconformities. Using this RGT image, we obtain an improved flattened image (Figure 8d), in which seismic reflectors are horizontally flattened and unconformities appear as vertical gaps.

Figure 9 shows a 3D example with two unconformity surfaces, highlighted by unconformity likelihoods in Figure 5. Using the two unconformity surfaces (Figure 5b) as constraints, we compute a reasonable RGT volume (Figure 9a) with obvious discontinuities at unconformities. We then use this RGT volume to compute a flattened image or 3D seismic Wheeler volume (Figure 9b), in which the unconformities are represented as vertical gaps or hiatuses and

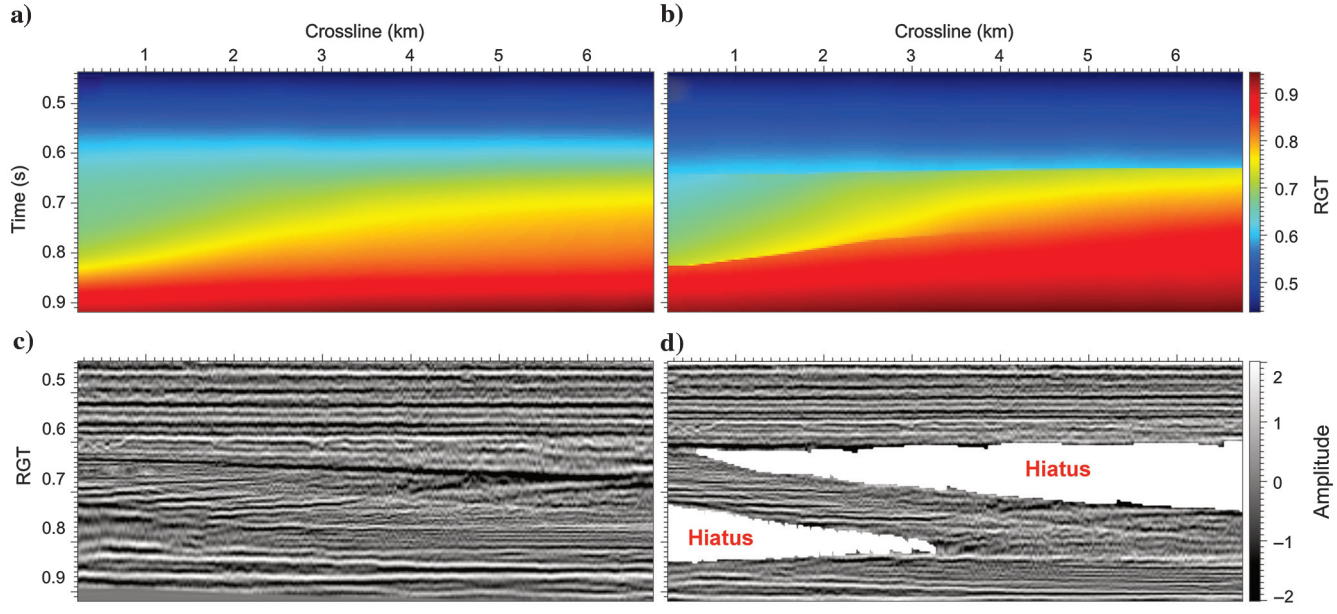

Figure 8. (a) An RGT, (c) flattened images generated with inaccurate seismic normal vectors (Figure 7a and 7c) and without unconformity constraints, (b) improved RGT, and (d) flattened images with more accurate seismic normal vectors (Figure 7b and 7d) and constraints from unconformity likelihoods (Figure 4).

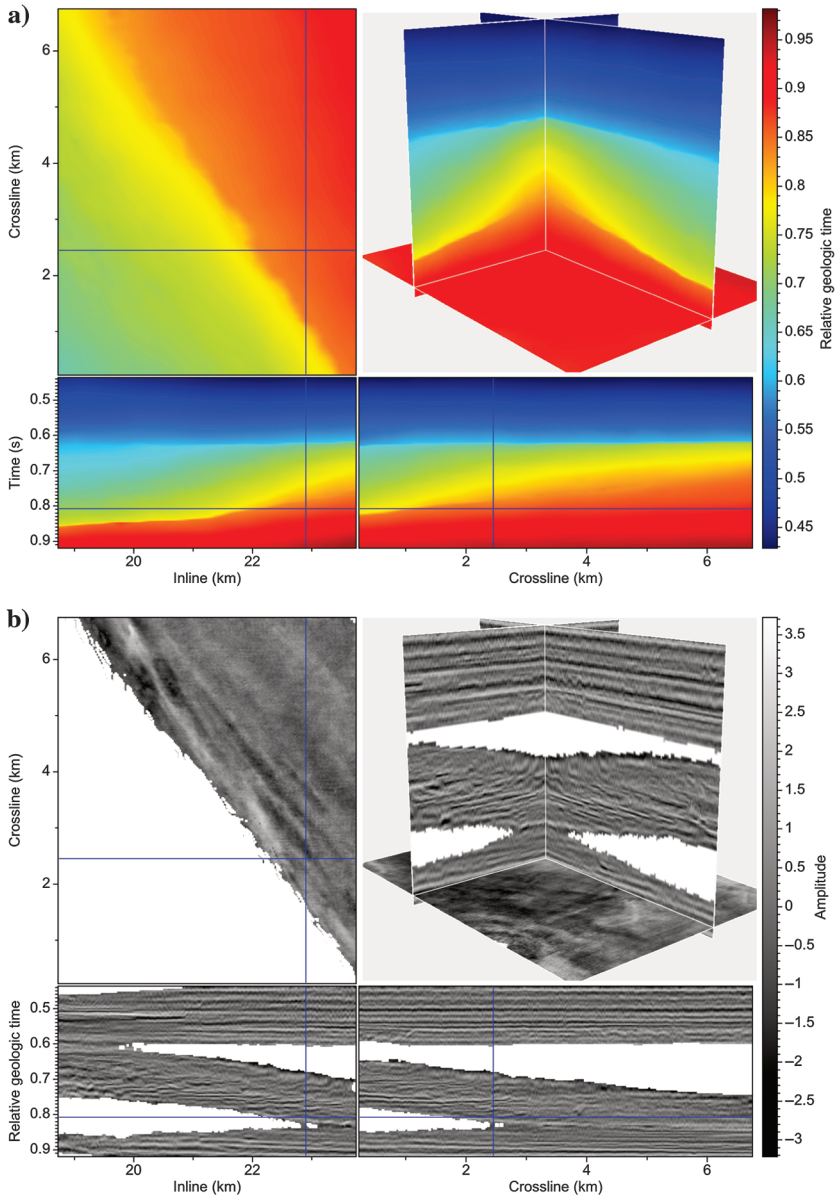

Figure 9. (a) Generated RGT volume and (b) flattened 3D seismic image. Discontinuities in the RGT volume correspond to vertical gaps or hiatuses (blank areas in panel [b]) in the flattened image at unconformities.

all seismic reflectors are flattened. The time slice of an RGT image shows large RGT variations between samples in the lower-left and upper-right areas that are separated by an unconformity. This indicates that the sediments, represented by the samples in the two different areas, are deposited in two different sedimentary sequences occurring at different geologic ages.

CONCLUSION

We have proposed a method to obtain an unconformity likelihood attribute from the differences between two seismic normal vector fields estimated from two structure-tensor fields, one is computed using a vertically causal smoothing filter, and the other using a vertically anticausal filter. From a seismic image, we first compute smoothed outer products of image gradients by applying a structure-oriented smoothing filter to each element of these outer products. These smoothed outer products are then smoothed using vertically causal and anticausal filters to compute two different structure-tensor fields, and their corresponding normal vector fields.

Using structure-oriented smoothing filters for the outer products, we extend structure variations from a termination area to the corresponding parallel unconformity and correlative conformity. In doing this, we assume that the correlative conformity or parallel unconformity is not dislocated by faults. If faults appear in the seismic image, we could perform unfaulting before attempting to detect unconformities.

We use separate vertically causal and anticausal filters to obtain structure tensors that differ at unconformities. Unconformity likelihoods might be further improved by instead using causal and anticausal filters that smooth in directions orthogonal to unconformities.

As examples of applications, we have shown how to estimate more accurate seismic normal vectors and better flatten seismic reflectors at unconformities using unconformity likelihoods as constraints.

ACKNOWLEDGMENTS

This research is supported by the sponsor companies of the Consortium Project on Seismic Inverse Methods for Complex Structures. All of the real seismic images used in this study are extracted from the F3 seismic data that were graciously provided by dGB Earth Sciences B.V. through OpendTect.

REFERENCES

Bahorich, M., and S. Farmer, 1995, 3-D seismic discontinuity for faults and stratigraphic features: The coherence cube: The Leading Edge, **14**, 1053–1058, doi: 10.1190/1.1437077.

Barnes, A. E., 2000, Attributes for automating seismic facies analysis: 70th Annual International Meeting, SEG, Expanded Abstracts, 553–556.

De Groot, P., A. Huck, G. de Bruin, N. Hemstra, and J. Bedford, 2010, The horizon cube: A step change in seismic interpretation: The Leading Edge, **29**, 1048–1055, doi: 10.1190/1.3485765.

Fehmers, G. C., and C. F. Höcker, 2003, Fast structural interpretation with structure oriented filtering: Geophysics, **68**, 1286–1293, doi: 10.1190/1.1598121.

Fomel, S., 2002, Applications of plane-wave destruction filters: Geophysics, **67**, 1946–1960, doi: 10.1190/1.1527095.

Hale, D., 2006, Recursive Gaussian filters: Center for Wave Phenomena, Report CWP-546.

Hale, D., 2009, Structure-oriented smoothing and semblance: Center for Wave Phenomena, Report CWP-635.

Hale, D., 2011, Structure-oriented bilateral filtering: 81st Annual International Meeting, SEG, Expanded Abstracts, 3596–3600.

Hale, D., 2012, Methods to compute fault images, extract fault surfaces, and estimate fault throws from 3D seismic images: Geophysics, **78**, no. 2, O33–O43, doi: 10.1190/geo2012-0331.1.

Hoek, T. V., S. Gesbert, and J. Pickens, 2010, Geometric attributes for seismic stratigraphic interpretation: The Leading Edge, **29**, 1056–1065, doi: 10.1190/1.3485766.

Lomask, J., A. Guitton, S. Fomel, J. Claerbout, and A. A. Valenciano, 2006, Flattening without picking: Geophysics, **71**, no. 4, P13–P20, doi: 10.1190/1.2210848.

Luo, S., and D. Hale, 2013, Unfaulting and unfolding 3D seismic images: Geophysics, **78**, no. 4, O45–O56.

Parks, D., 2010, Seismic image flattening as a linear inverse problem: Master's thesis, Colorado School of Mines.

Ringdal, K., 2012, Flow-based segmentation of seismic data: Master's thesis, University of Bergen.

Smythe, J., A. Gersztenkorn, B. Radovich, C.-F. Li, and C. Liner, 2004, Gulf of Mexico shelf framework interpretation using a bed-form attribute from spectral imaging: The Leading Edge, **23**, 921–926, doi: 10.1190/1.1803504.

Vail, P. R., R. G. Todd, and J. B. Sangree, 1977, Seismic stratigraphy and global changes of sea level — Part 5. Chronostratigraphic significance of seismic reflections: Section 2 — Application of seismic reflection configuration to stratigraphic interpretation, *in*, C. E. Payton, ed., Seismic Stratigraphy — Applications to Hydrocarbon Exploration, AAPG Memoir, vol. 26, 99–116.

Van Vliet, L. J., and P. W. Verbeek, 1995, Estimators for orientation and anisotropy in digitized images: ASCI'95, Proceedings of the First Conference of the Advanced School for Computing and Imaging.

Wu, X., and D. Hale, 2014, Horizon volumes with interpreted constraints: Center for Wave Phenomena, Report CWP-812.

Wu, X., and G. Zhong, 2012a, Generating a relative geologic time volume by 3D graph-cut phase unwrapping method with horizon and unconformity constraints: Geophysics, **77**, no. 4, O21–O34, doi: 10.1190/geo2011-0351.1.

Wu, X., and G. Zhong, 2012b, A method for generating a seismic Wheeler volume via a relative geologic time volume: 82nd Annual International Meeting, SEG, Expanded Abstracts, doi: 10.1190/segam2012-1177.1.